

# Enhancing 9 nm Node Dense Patterned Defect Optical Inspection using Polarization, Angle, and Focus

Bryan M. Barnes\*, Francois Goasmat, Martin Y. Sohn, Hui Zhou, and Richard M. Silver  
Physical Measurement Laboratory, National Institute of Standards and Technology,  
100 Bureau Dr. MS 8212, Gaithersburg, MD USA 20899-8212

Abraham Arceo  
SEMATECH, 257 Fuller Rd. Ste. 2200, Albany, NY 12203

## ABSTRACT

To measure the new SEMATECH 9 nm node Intentional Defect Array (IDA) and subsequent small, complex defects, a methodology has been used to exploit the rich information content generated when simulating or acquiring several images of sub-wavelength-sized defects through best focus. These images, which are  $xy$  planes, collected using polarized illumination are stacked according to focus position,  $z$ , and through interpolation, volumetric pixels (“voxels”) are formed sized approximately 40 nm per side. From the image data, an intensity can be assigned to each  $(x,y,z)$  position. These four-dimensional matrices are extensively filtered for defect detection using multi-dimensional intensity thresholding, nearest-neighbor criteria, continuity requirements, and other techniques standard to optical defect inspection. A simulation example with oblique angles of illumination is presented. Experimental results are shown from the NIST  $\lambda=193$  nm Microscope using full-field illumination. Volumetric data analysis is compared against the processing of single 2-D images. Defect metrics for comparing planar and volumetric data are developed with the potential shown for a five-fold increase in defect sensitivity using volumetric data versus conventional imaging.

**Keywords:** Defect detection, Scatterfield optical microscopy, bright-field microscopy, dark-field microscopy, volumetric imaging

## 1. INTRODUCTION

Optical defect inspection grows more challenging as critical dimensions decrease and circuit intricacy increases. This complexity, in addition to the variation (or inhomogeneity) of the features, gives rise to what is called wafer noise [1]. Optical scattering due to wafer noise can manifest itself during defect detection, and separating out such noise from actual defectivity is of utmost importance. Such progress will only come from continually refining methods for optimizing the detection of patterned defects sized well below the wavelength of the light. In this paper, extensive modeling and measurement of an Intentional Defect Array (IDA) from SEMATECH provides valuable insight into the upcoming 9 nm manufacturing node and motivates the description of a methodology to exploit the rich information content generated when acquiring several images of sub-wavelength-sized defects through best focus.

Our group at the National Institute of Standards and Technology (NIST) has been addressing such manufacturing requirements through the development of novel optical techniques such as Scatterfield Optical Microscopy (SOM). As defined in the initial publication of scatterfield, the methodology uses “structured or engineered illumination in an optical system with conventional high numerical aperture (NA) collection optics ... tailored to the target of interest. ... The combination of the structured illumination and target results in a three-dimensional interference field above the sample.”[2] Stepping through focus in a Köhler illuminated system has been integral to the scatterfield approach for metrology of the three-dimensional scattered electromagnetic field, and more recently the study of perturbations of that field due to defects.

We have previously reported simulations and experiments on the detectability of certain defect types for the 65 nm node, 32 nm node, and 22 nm node SEMATECH Intentional Defect Arrays (IDA),[3-5] with focus-resolved results shown for the 65 nm and 22 nm nodes. Defect detectability metrics were plotted as functions of polarization  $p$ , focus height  $z$ ,

\*bryan.barnes@nist.gov; phone 1 301 975-3947; fax 1 301 975-4396; www.nist.gov/pml/div683/grp02/htnsm.cfm

polar incident angle  $\theta$ , and illumination wavelength  $\lambda$ , for simulations of the 65 nm node. In general, best focus for defect detection varied little outside a range of -500 nm to 500 nm about the substrate.[3] Both focus-resolved simulations and experiments were performed for the 22 nm IDA. Images of defects bridging adjacent lines were plotted for several focus positions with the linear polarization aligned with the bridge direction in all cases. Aligning the polarization to match the direction of these highly directional defects yielded better detectability throughout the focus range. The experimental focus-resolved data emphasized the importance of noise on the images and the importance of proper image alignment.[5]

In the work above, several slices and areas of the three-dimensional scattered field were presented to yield a greater understanding of the interplay among polarization, wavelength, incident angle, and focus position in increasing defect detection. Two-dimensional treatments of the data cannot fully utilize this information. In this paper, we will quantify and rigorously use three-dimensional focus information volumetrically, correlating the two-dimensional images with their known focus positions to form a three-dimensional matrix, operating on the scattering from the defect as a multi-dimensional object. This multi-dimensional defect detection methodology will be explored in Section 3, after a discussion in Section 2 on recent three-dimensional patterned defect electromagnetic simulations using polarization, incident angle, and focus position.

In Section 4, measurements from the NIST  $\lambda=193$  nm Microscope are presented using this methodology on the SEMATECH 9 nm node IDA, demonstrating up to a five-fold increase in experimental defect sensitivity compared to conventional two-dimensional imaging. Though the 193 nm Tool is a “scatterfield-capable” platform with an accessible conjugate to the back focal plane (CBFP), in the work presented here this plane was not manipulated for target-specific structured illumination. The majority of the work presented could be replicated on any Köhler illuminated microscope with fine (nanometer scale) control of focus position, minimizing the need for additional hardware.

## 2. THREE-DIMENSIONAL DEFECT SIMULATION

The SEMATECH IDA provides a matrix of several defect types and various programmed sizes nominally near the 9 nm design rule. Three defect types here are explored, shown schematically in Fig. 1. The “Bx” defect joins lines end-to-end along the  $x$  direction, while the “By” defect connects adjacent lines with a perpendicular bridge. The “J” defect is a line intrusion as shown.

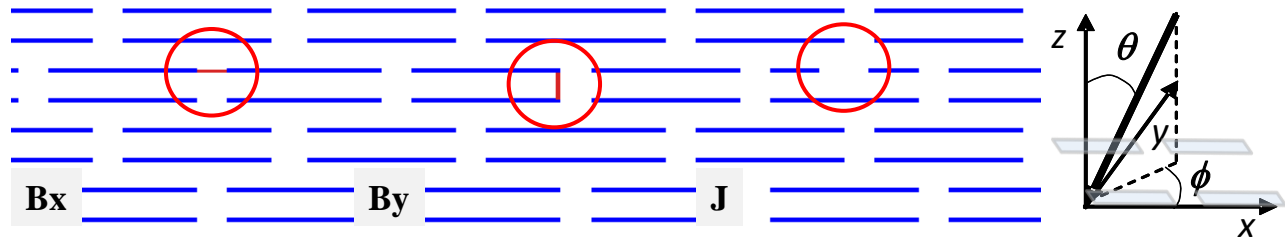


Figure 1. (left) Schematics of three types of highly directional defects. At far left is the “Bx” bridge connecting two lines end-to-end. The “By” defect is shown at center, bridging two parallel adjacent lines. The “J” defect at the right is a line break. Simulations were performed with one defect per domain with each domain sized  $2.16 \mu\text{m} \times 2.16 \mu\text{m}$ , a  $3 \times 9$  repetition of the unit cell. The finite difference time domain (FDTD) grid size was 3 nm with simulation wavelength  $\lambda = 193$  nm. (right) Definitions of polar ( $\theta$ ) and azimuthal ( $\phi$ ) angles and the  $xyz$  coordinate system relative to the simulation layout.

The modeling of scattering from defect targets requires the use of three-dimensional electromagnetic simulators. Simulations of each defect are performed at various incident polar and azimuthal angles using a finite difference time domain (FDTD) [6] electromagnetic model. The microscope is assumed to be Köhler illuminated with  $\lambda=193$  nm, with plane waves at the sample. For defect analysis, two simulation sets are performed: one with a patterned defect, one without. The result of each simulation is an aerial image at a particular focus height  $z$ . To produce Fig. 2 below, 79 simulation sets per defect per polarization were performed using a concentric sampling strategy.[7] The defect-containing and defect-free images are subtracted to determine the difference in the scattered field due to the defect, called a defect signal. Random and correlated noise, with  $3\sigma_{\text{noise}} = 2\%$  of the incident intensity  $I_0$ , is added to each

difference image. The absolute value image was reduced to a single mean value to provide a figure-of-merit (FOM) that is then plotted as a function of the incident angles.

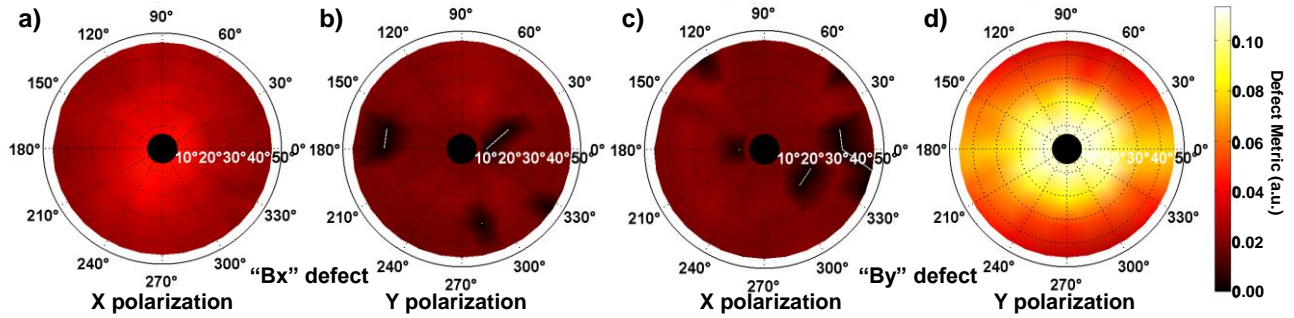


Figure 2. Simulated polar plots of a defect metric for the four possible combinations of X- and Y-polarization and 8 nm-wide “Bx” and “By” bridge defects as defined in Fig. 1. Intensities shown are of a defect detectability figure-of-merit described in the text. Simulations were performed for critical dimensions of 89 % of the 9 nm design rule (DR) and  $\lambda = 193$  nm light using an in-house (FDTD) model. Detectability is enhanced by aligning the polarization along the bridge direction. Small ( $\theta < 20^\circ$ ) polar angles are preferable to larger ( $\theta > 30^\circ$ ) angles. There is also a modest benefit to aligning the incident azimuthal plane perpendicular to the bridge. Plots are shown at optimal focus positions for each defect,  $z = -200$  nm below the substrate for Bx,  $z = 100$  nm above for “By”.

In Fig. 2, the data show that the strongest defect detectability should be for the “By”-type defect, illuminated using linearly polarized light aligned with the defect. Similarly, for the “Bx” defect, the detectability is also stronger when the linear polarization is aligned along the defect. These highly directional bridges are quite sensitive to polarization. With respect to incident angle, there is a trend toward higher detectability for smaller values of the polar angle,  $\theta$ . The azimuthal angle  $\phi$  has a slight effect, with the “Bx” defect more detectable using  $\phi = 90^\circ$  and  $\phi = 270^\circ$  while “By” is more detectable using  $\phi = 0^\circ$  or  $\phi = 180^\circ$ . These angular tendencies are more modest than the clear trends found previously for the 22 nm SEMATECH IDA.

All 79 simulations can be used together to simulate the full-field illumination from the NIST 193 nm Microscope, the optical platform used in these experiments. Dipole illumination can be simulated using a subset of these simulations, as was done to illustrate a multi-dimensional defect detection approach outlined below.

### 3. MULTI-DIMENSIONAL DEFECT DETECTION

One simulation of a dipole-illuminated, 8 nm-wide “Bx” defect is shown in Fig. 3 to illustrate a volumetric approach for analyzing focus-resolved data. In this example, one bridge defect is placed near the center of a layout spanning  $2.16 \mu\text{m} \times 2.16 \mu\text{m}$  along  $x$  and  $y$  directions. After modeling the electromagnetic scattered field, images are generated throughout an approximately  $2 \mu\text{m}$  range in  $z$ . An individual pixel in an image has a single intensity correlated to a specific  $xy$  position. Likewise, using cubic volumetric pixels (“voxels”) in  $xyz$  space, a single intensity for each voxel can be found, yielding a four-dimensional matrix of spatial and intensity information.

As described in the previous section, differential defect analysis requires defect-containing and defect-free image information. Two separate volumes are constructed, one with the defect and one as a reference. The center of Fig. 3 shows a graphical representation of this defect volume. Subtraction of the defect and reference volumes yields a difference volume. Adding random and correlated noise to each  $xy$  plane of voxels, a difference volume is obtained and shown as Fig. 3(b). This noise addition emulates the types of noise encountered during measurements at  $\lambda = 193$  nm due to speckle and camera noise, for example.

This difference matrix permits full use of three-dimensional filtering, intensity thresholding, and continuity requirements for optimizing defect detection in addition to standard image-based detection methods. The volume in Fig. 3(b) can be divided into sub-volumes as shown in Fig. 3(c). This rendering identifies all sub-volumes of voxels having 26 nearest neighbors having intensities greater than 3.5 times the standard deviation of all intensities in the volume. The green regions indicate sub-volumes due to defect scattering as opposed to “noisy” regions labeled in red. The primary

identifier of the defect in this example is the continuity of the defect throughout focus, over a range of  $z$  values. The defect and its location are of course known *a priori* as this is an illustration from simulation. The analytical advantages and challenges will now be demonstrated using experimental data.

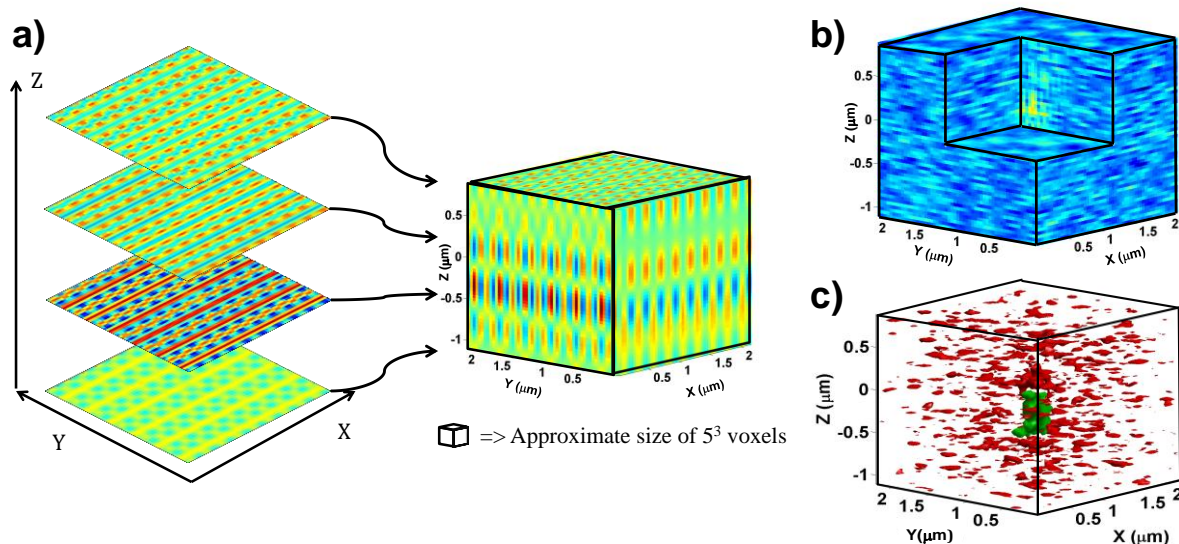


Figure 3. (color online) (a) Schematic construction of the volumetric image. Individual images, with pixels yielding  $(x, y, I)$  are collected through-focus and stacked within a four dimensional  $(x, y, z, I)$  volume. Only four slices are shown at left of the fifty-two comprising the center volume. In this simulation example, the volumetric pixels, or “voxels” are  $39 \text{ nm} \times 39 \text{ nm} \times 39 \text{ nm}$ . For scale, a cubic sub-volume of 125 ( $5^3$ ) voxels is shown at bottom center. (b) Simulated difference volume with random and correlated noise added on each  $xy$  image plane. The  $3\sigma$  magnitude of the noise is 6.0 % of the incident intensity. The cut-out shows a portion of the change in intensity that extends throughout an extended  $z$  range due to the presence of a defect. (c) Simulated defect detection for bridge defect “Bx” of nominal size 8 nm using volumetric methods. Regions in red and green envelop volumes with intensities greater than  $3.5\sigma$ . The green volume is associated with a defect due to the three-dimensional continuity of the defect over prescribed lengths in  $x$ ,  $y$ , and  $z$  as well as meeting certain nearest-neighbor requirements. The red volumes fail these continuity tests and are excluded as noise.

## 4. EXPERIMENTAL MEASUREMENTS AND ANALYSIS

### 4.1. A Volumetric Example from Focus-resolved Measurements

This methodology has been applied to images collected from several of the “Bx”, “By”, and “J” defects on a SEMATECH IDA wafer coupon measured using the NIST  $\lambda = 193 \text{ nm}$  Microscope [8]. Difference volumes were generated from a defect volume and a reference volume as in simulation. In these experiments however, the shift between the “reference” and “defect” volumes is less than one micrometer; thus the defect is found in the field-of-view of both measurement sets. This differential shifting method yields a duplicate copy of the defect in the absolute value of the difference volume, as shown at the far left of Fig. 4 below.

The formation of the difference volume is non-trivial, and the performance of this operation determines the effectiveness of the measurement. First, the intensity of each image is normalized against an intensity reference camera that is synchronized to the imaging camera. This intensity reference minimizes the effects of laser flicker and power fluctuation upon the measurement. Second, three-dimensional Fourier intensity filtering is performed on both the reference and defect volumes. A low frequency filter was applied to each volume, removing constant backgrounds and large variations in these volumes. A high-frequency filter was also applied to isolate the repetitive structure of the defects from the noise in the volumes, and a three-dimensional inverse discrete Fourier transformation of the filtered volumes is performed. Third, the two volumes have to be correlated in all three dimensions. It is important to note that our choice of cubic voxels was made to simplify this three-dimensional Fourier filtering. The number of positions

needed to adequately represent changes in intensity with respect to  $z$  throughout the volume, and the  $z$  spacing used to store this information need not be tied to the  $xy$  dimensions of the camera pixels used for data collection.

In hardware, every attempt is made to maintain the  $z$  position between reference and defect images, and the offset along  $x$  is determined by the periodicity of the structure. Despite these best efforts, subpixel-sized misalignment will occur. To treat these data, we have used a three-dimensional implementation of the Enhanced Correlation Coefficient (ECC) algorithm of Evangelidis and Psarakis.[9] In a full ECC treatment, a matrix is produced to warp one volume to maximize its correlation with a second volume. Here, only the lateral shift elements of this matrix are used to perform the sub-pixel interpolation required to align the images, leaving the shape and dimensions of the images intact.

With this 3-D difference matrix, we are now in a position to exploit the benefits from 3-D continuity, 3-D filtering, 3-D thresholding, as well as employing other defect detection methods over the full volume. The initial steps to identify the defect in Fig. 4 below include thresholding by intensity and enforcing nearest-neighbor requirements. A complete rendering of the difference volume for a “J” defect is shown. A  $7.5 \sigma$  intensity threshold has been established for all experimental data presented. Filtering by size in  $x$ ,  $y$ , and  $z$  and by total volume, two defect signatures were identified and its centroid location determined.

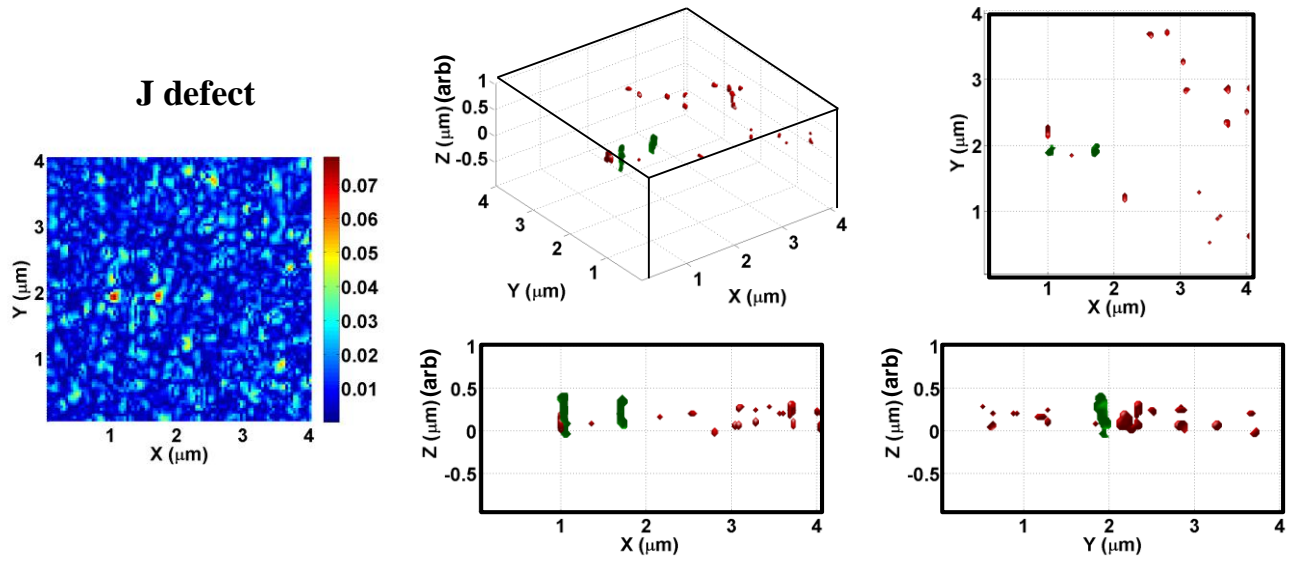


Figure 4. Five views of the differential volume measured for a “J” (line intrusion) defect on the first measured die. As the defect volume and reference volume are shifted by less than  $1 \mu\text{m}$ , two copies of the defect are visualized. Clockwise from top center, a 3-D isometric view is shown of the differential volume with the two defect signatures marked by green volumes. A top down  $xy$  projection shows these defects near the  $y = 2 \mu\text{m}$  line. An  $yz$  projection shows a single defect as its copy is hidden behind. Both defects are seen again in the  $xy$  projection. At far left is an  $xy$  slice through the volume at the  $z$  centroid of one of the defect volumes. The two copies of the defect are clearly visible in this example of experimental volumetric data.

#### 4.2. Qualitative Comparisons among Several Defects

Two IDA dies on a single wafer coupon were inspected for this initial experimental study at the 9 nm node. The coupon was etched using e-beam lithography with a focus-exposure matrix, leading to a variation of die quality across the coupon. The first die measured was well patterned as observed using scanning electron microscopy (SEM), while the second die was used to test the effects of lower quality patterning on defect detection. The “J” defect measured in Fig. 4 was from this 1<sup>st</sup> die. These arrays offer a matrix of defect types and defect sizes nominally scaled to the 9 nm design rule, with schematics of some of these defects presented previously as Fig. 1. Survey inspection of the defects presented here was performed using Scanning Electron Microscopy (SEM) to assess defect printing quality.

Figure 5 shows measurements of two “By” bridge defects paired to highlight the effects of printing quality, polarization, and defect size on detectability with this volumetric approach. In Fig. 5(a), the nominally smallest “By” defect in the 1<sup>st</sup>

die is shown in the SEM image. The critical dimension of this defect is  $17 \text{ nm} \pm 3 \text{ nm}$  ( $k=1$ ). One transmission electron micrograph of a patterned line from a sibling wafer of this IDA array indicates that the middle width may be approximately half the width of the linewidth at the base, but without additional information we assume a constant width of the defect. The incident intensity is full-field illumination with polarization aligned along the bridge direction. Using the volumetric treatment, the defect volumes are easily observed for the “By” defect from the 1<sup>st</sup> die, and the two defect spots are readily visible in the two-dimensional slice at far left.

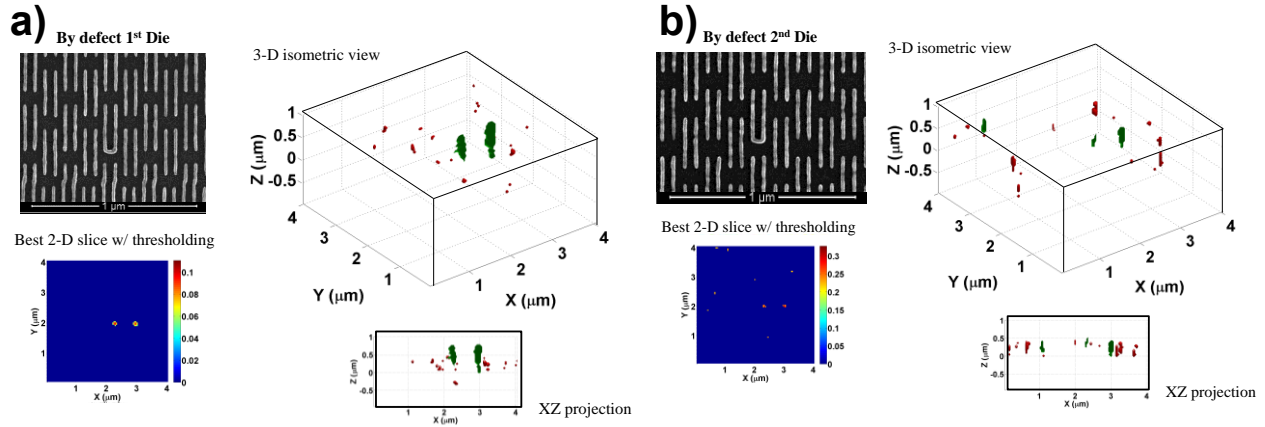


Figure 5. “By” bridge defects with different nominal sizes from two different dies. (a) SEM image of a defect on the 1<sup>st</sup> die and its volumetric difference optical scattering data in both 3-D isometric view and  $xz$  projection. The defect is easily identified in both 2-D and 3-D representations. (b) SEM image of a defect on the 2<sup>nd</sup> die and its difference data. Here, the defect is not easily identified using just one 2-D slice.

This is to be contrast with the measurement of a “By” defect on the 2<sup>nd</sup> die in Fig. 5(b). The linear polarization is aligned perpendicular to the bridge. This orientation is not optimal, but chosen to illustrate further defect detection under less optimal conditions. The nominal critical dimension is  $4 \text{ nm}$  wider than bridge in Fig. 5(a). The SEM again indicates a critical dimension of  $17 \text{ nm} \pm 3 \text{ nm}$  ( $k=1$ ) and the patterning fidelity is slightly degraded.

While the number of sub-volumes in Fig. 5(b) is similar to the number in Fig. 5(a), more continuity in the  $z$ -direction is observed for some sub-volumes in the  $xz$  projection in this latter example, consistent with small intensity fluctuations due to the subtraction of scattering from imperfectly patterned layers. The “By” defect here is still identified near the  $x = 3 \mu\text{m}$  plane, with an additional positive defect indicated near  $(x, y) = (1 \mu\text{m}, 3 \mu\text{m})$ . There is a smaller “noise” volume offset from this additional defect that indicates that it may indeed be an observation of another wafer-based defect. A best  $xy$  slice as determined from the volumetric approach is also shown in Fig. 5(b). Several points in addition to the programmed defect and even the possible additional defect surpass the threshold at this plane. Use of the full three dimensional scattered data and  $z$  dimensional continuity information facilitates identifying and locating defects.

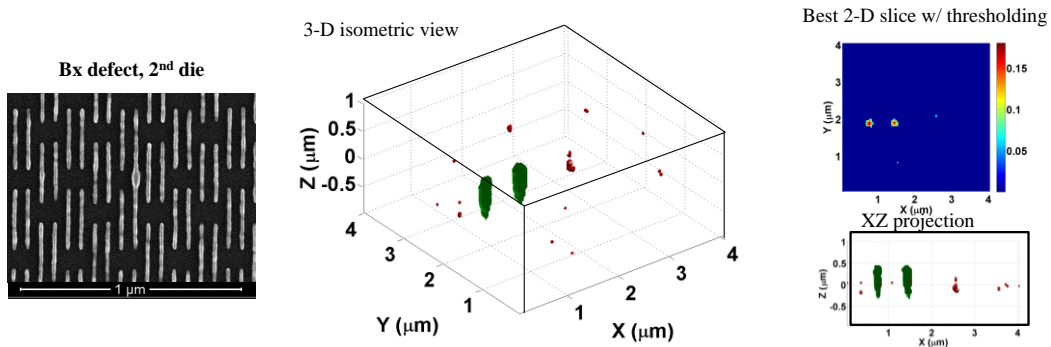


Figure 6. A relatively wide “Bx” bridge defect on the 2<sup>nd</sup> die illuminated using full-field illumination with its linear polarization oriented orthogonal the bridge direction.

In simulation, it was predicted that the detectability of both the “Bx” and “By” bridges would be enhanced by aligning the incident polarization along the bridge direction. This was also predicted by simulation and observed experimentally for the 22 nm node IDA.[5] Measurements were performed using both *X* and *Y* polarized light on the “By” bridges in Fig. 5 and on the “Bx” bridge in Fig. 6. As mentioned above, the results from polarization perpendicular to the “By” defect (*X* polarization) were shown in Fig. 5(b) in order to make the measurement more difficult. For both dies in Fig. 5, the *Y* polarization, along the bridge direction, was optimal. In Fig. 6, the defectivity of the “Bx” bridge is shown using *Y* polarization as it is optimal also, although it is orthogonal to the bridge direction. This apparent switching of the optimal polarization axis for this particular “Bx” bridge is likely due to the relatively large width of the defect in the *Y* dimension,  $CD = 33 \text{ nm} \pm 4 \text{ nm}$  ( $k=1$ ).

### 4.3. Quantitative Comparisons to Two-dimensional Imaging

It is important to compare image-based metrics against volume-based metrics using units common to both. Qualitatively, defect detection is a binary exercise and instances where a 2-D slice would suffice have been identified while developing the multi-dimensional defect detection methodology. To perform a quantitative comparison of defect sensitivity between a single 2-D image and a 3-D volume, we have developed appropriate defect metrics such as the projection and integration of three-dimensional data onto a 2-D plane. For example, by flattening the *y* direction of the volume we project all identified voxels as pixels on the *xz* plane which permits a comparison of the projected area versus the above-threshold area in a single *xy* slice. Alternatively, during flattening the voxel intensities may be integrated corresponding to their *xz* positions. This also can be compared against the integrated intensity above a certain threshold in a specific *xy* plane. These two metrics (area and integrated intensity) are shown in Tables 1 and 2 respectively for the defects shown in Figs. 4, 5, and 6.

Table 1. Comparisons of an area-based defect metric between a 2-D and flattened projections of a 3-D volume. Defects “Bx”, “By” and “J” are each measured. The improvement in sensitivity between the 2-D and 3-D results ranges from a factor of 3.8 to a factor of 6.0, varying with defect type and 3-D projection direction.

	Area (pixels <sup>2</sup> )			
	2 <sup>nd</sup> Die, “Bx” Y pol. 1.33 DR	1 <sup>st</sup> Die, “By” Y pol. 0.45 DR	2 <sup>nd</sup> Die, “By” X pol. 0.89 DR	1 <sup>st</sup> Die, “J” Y pol. 1.55 DR
2-D Best Image	21	12	5	8
3-D, Flatten <i>x</i>	88	72	27	42
3-D, Flatten <i>y</i>	96	69	18	42

Table 2. Comparisons of an integrated intensity defect metric between a 2-D and flattened projections of a 3-D volume. In this initial study, integration was performed after the volumetric identification thus both the *xz* and *yz* projections yield the same value. The improvement in sensitivity between the 2-D and 3-D results varies with defect type, ranging by a factor of 7.5 up to a factor of 14.9.

	Integrated Intensity (a.u.)			
	2 <sup>nd</sup> Die, “Bx” Y pol. 1.33 DR	1 <sup>st</sup> Die, “By” Y pol. 0.45 DR	2 <sup>nd</sup> Die, “By” X pol. 0.89 DR	1 <sup>st</sup> Die, “J” Y pol. 1.55 DR
2-D Best Image	2.30	0.87	1.29	0.50
3-D, Flatten <i>x</i>	31.49	12.96	9.79	6.03
3-D, Flatten <i>y</i>				

In Table 1, the addition of the focus-resolved data increases the defect sensitivity using an area-based defect metric by about a factor of five or more for at least one of the two 3-D projections used. The integrated intensity metric in Table 2 shows an even greater sensitivity. As several measurements of this 9 nm IDA showed clear defectivity in just the 2-D images, identifying the appropriate applicability of this volumetric treatment to a defect problem must be addressed. In contrast to this IDA which was printed on one level, in high-volume semiconductor manufacturing there are several layers in the process stack, and defect detection is hindered by the additional scattering from underlayers. This complexity, in addition to the roughness and variation of the features, gives rise to wafer noise as noted previously and

unwanted correlations throughout the  $xyz$  space are to be expected, but likely can be reduced using this 3-D differential volumetric approach. Continued defect detection given these difficulties is an ongoing challenge potentially addressed through this methodology.

## 5. CONCLUSIONS

A multi-dimensional defect detection methodology was demonstrated using both simulation and experimental results from the SEMATECH 9 nm node IDA. This approach was shown to be an extension of scatterfield optical microscopy techniques that may be implemented on existing platforms without requiring major tool redesigns. Data acquisition was thus concentrated on focus-resolved measurements using full-field illumination and linearly polarized light. Bridge defects “Bx”, “By” and line intrusion “J” were all used to illustrate this methodology. Qualitatively, many measurements of these single-level defects yielded a best detectability  $z$  position from which defects could be determined in a single  $xy$  image. For these defects, the volumetric approach yielded an almost five-fold increase in sensitivity using an area-based focus metric. An increasing number of focus positions may need to be measured to address wafer noise as dimensions decrease, and this volumetric methodology is well-positioned for optimizing defect detection using this additional focus-resolved data.

## ACKNOWLEDGEMENTS

The authors wish to thank the SEMATECH Metrology Initiative for access to these intentional defect array wafers. We also thank Andras Vladar and Bin Ming for assistance in SEM measurements.

## REFERENCES

- [1] T. F. Crimmins, "Wafer noise models for defect inspection," Proc. SPIE 7971, 79710E (2012).
- [2] R. M. Silver, R. Attota, M. Stocker, M. Bishop, L. Howard, T. Germer, E. Marx, M. Davidson, and R. Larrabee, "High-resolution optical metrology," Proc. SPIE 5752, 67-79 (2005).
- [3] R. M. Silver, B. M. Barnes, Y.-J. Sohn, R. Quintanilha, H. Zhou, C. Deeb, M. Johnson, M. Goodwin, and D. Patel, "The limits and extensibility of optical patterned defect inspection," Proc. SPIE 7638, 76380J (2010).
- [4] B. M. Barnes, R. Quintanilha, Y.-J. Sohn, H. Zhou, and R.M. Silver, "Optical illumination optimization for patterned defect inspection," Proc. SPIE 7971, 79710D (2011).
- [5] B. M. Barnes, Y.-J. Sohn, F. Goasmat, H. Zhou, and R. M. Silver, "Scatterfield microscopy of 22 nm node patterned defects using visible and DUV light," Proc. SPIE 8324, 83240F (2012).
- [6] A. Taflove, "Application of the finite-difference time-domain method to sinusoidal steady-state electromagnetic-penetration problems," IEEE Transactions on Electromagnetic Compatibility EMC-22, 191-202 (1980).
- [7] P. Shirley and K. Chiu, "A low distortion map between disk and square," J. Graphics Tools 2, 45-52 (1997).
- [8] Y.-J. Sohn, R. Quintanilha, B.M. Barnes, and R. M. Silver, "193 nm angle-resolved scatterfield microscope for semiconductor metrology," Proc. SPIE 7405, 74050R (2009).
- [9] G. D. Evangelidis and E. Z. Psarakis, "Parametric image alignment using enhanced correlation coefficient maximization," IEEE Trans. Pattern Analysis and Machine Intelligence 30, 1-8 (2008).

The full description of the procedures used in this paper requires the identification of certain commercial products and their suppliers. The inclusion of such information should in no way be construed as indicating that such products or suppliers are endorsed by NIST or are recommended by NIST or that they are necessarily the best materials, instruments, software or suppliers for the purposes described.